Plasma Physics and
Controlled Fusion

PAPER

2D distributions of potential and density mean-values and oscillations in the ECRH and NBI plasmas at the TJ-II stellarator

To cite this article: A V Melnikov *et al* 2022 *Plasma Phys. Control. Fusion* **64** 054009

IOP Publishing
Plasma Physics and Controlled Fusion
Plasma Phys. Control. Fusion **64** (2022) 054009 (10pp)
https://doi.org/10.1088/1361-6587/ac5b4c

2D distributions of potential and density mean-values and oscillations in the ECRH and NBI plasmas at the TJ-II stellarator

A V Melnikov[1,2,3,*], **L G Eliseev**[1], **J M Barcala**[4], **A Cappa**[4], **A A Chmyga**[5], **M A Drabinskiy**[1], **C Hidalgo**[4], **P O Khabanov**[1], **N K Kharchev**[1,6], **A S Kozachek**[5], **M Liniers**[4], **D López-Bruna**[4], **U Losada**[4], **S E Lysenko**[1], **F Medina**[4], **A Molinero**[4], **M Ochando**[4], **J L De Pablos**[4], **I Pastor**[4] **and TJ-II Team**[4,7]

[1] National Research Centre ‘Kurchatov Institute’, 123182 Moscow, Russia
[2] National Research Nuclear University ‘MEPhI’, 115409 Moscow, Russia
[3] Moscow Institute of Physics and Technology, 141700 Dolgoprudny, Russia
[4] Fusion National Laboratory, CIEMAT, 28040 Madrid, Spain
[5] Institute of Plasma Physics, NSC KIPT, 61108 Kharkov, Ukraine
[6] Prokhorov General Physics Institute, 119991 Moscow, Russia

E-mail: Melnikov_AV@nrcki.ru

Received 8 October 2021, revised 2 February 2022
Accepted for publication 7 March 2022
Published 12 April 2022

Abstract

2D plasma potential φ distribution was measured in the electron cyclotron resonance heating (ECRH) and neutral beam injection (NBI) plasmas of the TJ-II stellarator with the heavy ion beam probe for the whole radial range and wide area of the poloidal angle, and supported by Langmuir probe data at the edge. The whole operation domain for the on-axis ECRH was explored ($\bar{n}_e = 0.45$–0.8×10^{19} m^{-3}, $P_{EC} = 220$–470 kW), in addition, NBI plasmas with $\bar{n}_e = 0.9$–1.3×10^{19} m^{-3} and $P_{NBI} = 510$ kW were studied. In ECRH plasmas the density ramp-up is accompanied by the evolution of the potential from the bell-like to the Mexican hat profile, while the density profiles were flat or slightly hollow. The potential has the positive peak at the centre, and LFS-HFS (low field—high field sides) and up-down symmetry. Equipotential lines are consistent with vacuum magnetic flux surfaces. In the high-density NBI scenario, the φ profile was fully negative with a minimum up to -300 V at the centre, while at low-density ECRH plasma, φ has a maximum up to $+0.9$ kV at the centre. Fluctuations of potential and density are stronger in low-density scenarios and not poloidally symmetric. At the mid-radius (area of the maximum density), root mean square (RMS) of fluctuations were up to $\varphi \sim 15$ V at LFS vs $\sim$20 V at HFS; RMS $n_e \sim 2\%$ at LFS vs $\sim$3% at HFS. In the NBI plasmas with the density rise, the asymmetry decreases and finally vanishing at $\bar{n}_e = 1.2 \times 10^{19}$ m^{-3}. 2D distribution of the NBI-induced Alfvén eigenmodes (AEs) shows asymmetric ballooning structure: contrary to broadband turbulence, AE-associated potential perturbation dominates in the LFS with a factor up to 1.7 respect to the HFS. The electrostatic mode, excited in ECRH plasmas by suprathermal electrons also shows asymmetric structures: density perturbation dominates in the top-bottom direction compared to LFS-HFS direction.

---

[7] See the author list of report OV/3-5 by C Hidalgo *et al* at *28th IAEA Fusion Energy Conference (FEC 2020)* https://nucleus.iaea.org/sites/fusionportal/Shared%20Documents/FEC%202020/fec2020-preprints/preprint0969.pdf.

[*] Author to whom any correspondence should be addressed.

Keywords: TJ-II stellarator, plasma potential, fluctuations, 2D poloidal distribution, asymmetry

(Some figures may appear in colour only in the online journal)

---

1. Introduction

Upcoming fusion devices will explore plasma regimes that are far from present ones. Consequently, extrapolations from purely empirical data can be misleading and reliable data are required to validate models in existing plasma scenarios.

The characterization of plasma profiles and fluctuations is an important topic to understand and validate transport mechanisms in magnetically confined fusion plasmas. The search for asymmetries in edge plasma fluctuations has shown the importance of the curvature driven instabilities in the plasma boundary region [1] and gyrokinetic (GK) simulations in stellarators has exhibited a strong localization of unstable modes along the flux surface [2]. In addition, flux-surface variations of electrostatic potential driven by neoclassical mechanism can have a significant impact on high-Z impurity radial fluxes [3].

Another important factor contributing to the particle transport is the density gradient localization, which is closely connected to the fuelling mechanisms in next step devices. Plasma simulations have investigated the level of inward turbulent particle transport in inverted density gradient regions [4] but validation studies are still at preliminary level [5–8].

It is well known that electric fields and turbulence play an important role in phenomena like transition in confinement [9] and profile self-organization, therefore, turbulence may affect the performance of future fusion reactors.

Finally, controlling the amplitude of Alfvén eigenmodes (AEs) in fusion plasmas is a key issue for ITER and beyond, because the fast ion losses associated with these modes might be deleterious for plasma performance as well as in the development of integrated power exhaust scenarios. The 2D characterization of AEs can pave the way for a better understanding of their dynamics and control.

Heavy ion beam probe (HIBP) measurements of 2D profiles of potential and its fluctuations were performed at tokamaks and stellarators starting from 1990th [10–12].

In TJ-II, the first attempt to measure 2D spatial profiles of potential and fluctuations in electron cyclotron resonance heating (ECRH) scenarios was published in [5]. The present paper reports the characterization of 2D poloidal structures of plasma profiles and fluctuations in the enlarged spatial area and extended operational domain of ECRH and neutral beam injection (NBI) scenarios.

2. Experimental setup

TJ-II is a four-period heliac with a major radius $R_0 = 1.5$ m, minor radius $a = 0.22$ m, $B_0 = 0.95$ T equipped with various diagnostics and oriented to plasma transport and turbulence studies [13]. Experiments were performed in the standard magnetic configuration, usually referred as 101_42_64, which has a rather flat profile of rotational transform with $\iota\!\!\!-(0) \approx 1.54$ and $\iota\!\!\!-(a) \approx 1.62$. We use on-axis ECRH of plasmas with one or two gyrotrons, operating at the second harmonic extraordinary mode with 53.2 GHz and $P_{\mathrm{EC}} = 220$ and 470 kW, and heating by co-directed NBI ($P_{\mathrm{NBI}} = 510$ kW).

HIBP is a key diagnostic to study potential and electrostatic fluctuations in the core plasmas [14]. HIBP has been recently used to study broadband electrostatic turbulence [15] along with AEs [16] and electrostatic modes [17]. TJ-II is equipped with two HIBP systems (Cs^+ beam with energy $E_{\mathrm{b}} = 90$–150 keV) [18, 19]. It was recently extended to 176 keV with a beam current up to 300 μA [20]. 2D mapping experiment was performed with HIBP-II operating with secondary beamline #1 [21]. The Langmuir probe (LP) data supports the HIBP measurements at the plasma edge. When we compute the plasma potential φ from LP data, we use the standard procedure $\varphi = \varphi_{\mathrm{fl}} + 2.5\,T_{\mathrm{e}}$, where φ_{fl} is a floating potential and T_{e} is the electron temperature.

It is known that HIBP measurements of potential fluctuations are always local, while density fluctuations may be affected by the path integral effect (PIE) [22]. For the low-density range under study in TJ-II, the PIE on the density fluctuations is negligibly small [23].

HIBP schematic is presented in figure 1. Scanning of injection angle with $E_{\mathrm{b}} = 132$ keV allows us to change the sample volume (SV) location in the radial interval $-1 < \rho < +1$, which means from high field side (HFS) to the low field side (LFS) through the plasma axis and thus to obtain the full radial profile along the detector line in one shot [24] as presented in figure 2. Variation of the beam energy moves the detector line and thus allows us to cover the significant part of plasma vertical cross-section by detector grid, shown in figure 2. In comparison with previous measurements [5], we expand the 2D spatial area of measurement in a factor of 3 due to enlarged range of beam energy E_b based on the new power supply and exploration of the lower energy range based on the beam tuning experience. The increased beam current and finer beam focusing allows us to expand the operational window of plasma scenarios and improve the signal/noise ratio [20]. The more accurate measurements of positions of the HIBP hardware (source, deflecting plates and analyzer) at the TJ-II machine allows us to improve the accuracy of beam trajectories and SV radial reference.

3. Experimental results

Several the most typical TJ-II scenarios with ECR and NBI heated plasmas were explored with HIBP diagnostics:

(a) ECRH scenario started with low line averaged density $\bar{n}_{\mathrm{e}} = 0.47 \pm 0.02 \times 10^{19}$ m^{-3}, higher ECRH power $P_{\mathrm{EC}} \sim 455$ kW and $T_{\mathrm{e}}(0) = 1.6$ keV (stage 1) followed by

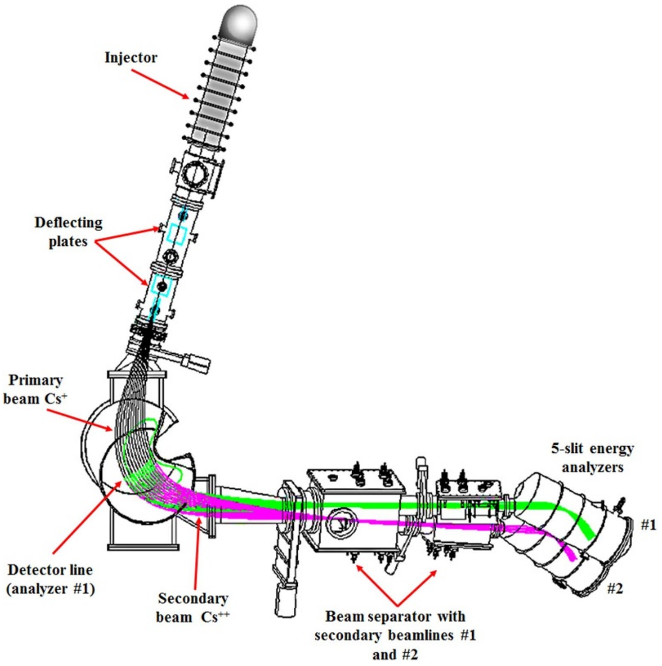

Figure 1. HIBP schematic.

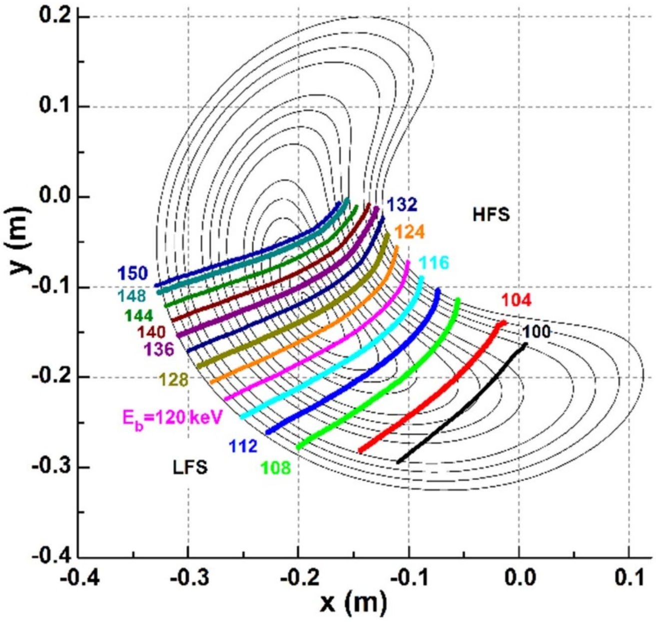

Figure 2. Detector lines of equal energies $E_b = 100$–150 keV, which can be obtained in one shot by scanning of injection angle are shown by different colours.

higher density $\bar{n}_e = 0.75 \pm 0.03 \times 10^{19}$ m^{-3}, lower on-axis ECRH, $P_{EC} = 220$ kW, and $T_e(0) = 1.4$ keV (stage 2);

(b) NBI scenario with an initial low-density ECRH stage replaced by co-NBI-only heated and sustained plasmas with rising density $\bar{n}_e = 1.0$–1.5×10^{19} m^{-3}, $P_{NBI} = 510$ kW, and $T_e(0) = 0.4$ keV;

(c) high-power ECRH scenario with very low line averaged density $\bar{n}_e = 0.32 \pm 0.02 \times 10^{19}$ m^{-3}, $P_{EC} \sim 540$ kW and $T_e(0) = 1.6$ keV, where hard x-ray measurements evidence suprathermal electrons existence [25].

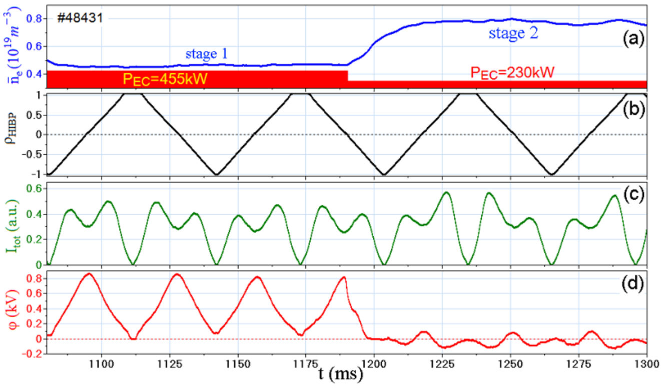

Figure 3. Scenario of experiment for the measurement of 2D maps: 1st stage (low $\bar{n}_e = 0.46 \times 10^{19}$ m^{-3}): ECRH1 + ECRH2 (455 kW), $T_e(0) = 1.6$ keV; 2nd stage (high $\bar{n}_e = 0.78 \times 10^{19}$ m^{-3}): ECRH1 (230 kW), $T_e(0) = 1.4$ keV; (a) line-averaged density; (b) SV position during HIBP scan; (c) secondary HIBP current proportional to local density; (d) the local plasma potential.

3.1. ECRH plasmas

Figure 3 shows the first on-axis ECRH scenario. The discharge has the first low-density stage with high ECRH power deposited by two gyrotrons, then the density increases by gas puffing, and the ECRH power was reduced, one gyrotron was switched off. The time trace of the line-averaged density is shown in the box (a). The box (b) shows the time evolution of the SV normalized radius ρ_{HIBP}. Periodic variation of ρ_{HIBP} from LFS ($\rho = 1$) to HFS ($\rho = -1$) allows us to get 3–4 reproducible profiles per stage. The time evolution of the total secondary beam current $I_{tot,}$ proportional to local density [26] and the plasma potential φ are shown in boxes (c) and (d) correspondingly. At the first stage, I_{tot} has hollow M-shaped trace, while the plasma potential looks like the chain of positive bell-shaped hills.

Figure 4 shows radial profiles of electron temperature (a), density (b) and plasma potential (c). We see that growth of density is accompanied by decrease of electron temperature that results in decrease of the central potential value and evolution of the potential shape from the bell-shape to Mexican hat with a small positive hill at the centre, the area of the ECRH power deposition. The density profiles are flat or slightly hollow in both stages. HIBP and LP data (solid lines and symbols at figure 4(c)) are consistent at the edge, $0.85 < \rho < 1$. Coincidence of double lines in figure 4(c) shows remarkable LFS-HFS symmetry of potential profiles.

The poloidal 2D map (figure 5(a), stage 1) shows that the local maximum of potential (up to about 0.9 kV) coincides with the plasma centre, and potential contours are consistent with the vacuum magnetic flux surfaces demonstrating (within experimental uncertainty) a poloidally symmetric structure. Such poloidal symmetry holds for stage 2 shown in figure 5(b).

Figures 6 and 7 show that the contour plot for root mean square (RMS) of plasma potential and density fluctuations

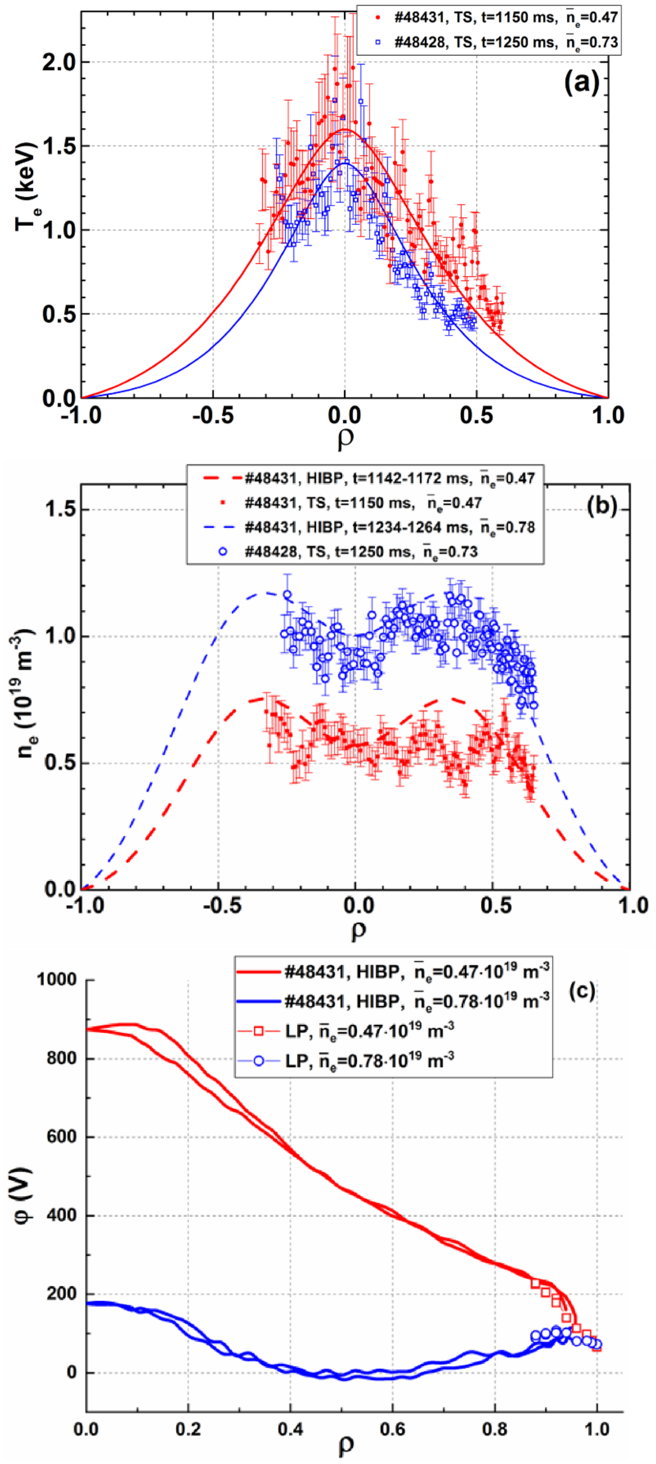

Figure 4. (a) The electron temperature profiles measured by Thomson scattering (points) and their fits (lines); (b) density measured by Thomson scattering (points) and HIBP (dashed lines); (c) profiles of potential measured by HIBP at $-1 < \rho < +1$ (lines) and LP (points). Stage 1 is in red, stage 2 is in blue.

with f < 300 kHz and k_ω < 3 cm^{-1} have more complicated shape: RMS distributions are not fully symmetric. The asymmetry is the most pronounced near mid-radius, where the density profile has a local maximum. Figure 6 shows that asymmetry is stronger for low densities: at the mid-radius, RMS $\varphi \sim 15$ V at LFS vs ~20 V at HFS, and the asymmetry factor for RMS φ at HFS/LFS is 1.33, while figure 7 shows that RMS $\delta n_e/n_e \sim 2\%$ at LFS vs ~ 3% at HFS, and the asymmetry factor is 1.5.

3.2. *NBI plasmas*

In addition to the ECRH plasmas, NBI scenario was explored, where the initial low-density ECRH stage was replaced to co-NBI-only heated and sustained plasmas (figure 8). NBI stage has line-averaged density $\bar{n}_e = 0.9$–$1.5\ \times 10^{19}$ m^{-3} The radial profile of plasma potential, measured over the central detector line with E_b = 132 keV is presented in figure 9(a). It has a shape of the negative potential well with maximal value at the plasma centre. Figure demonstrates the symmetry LFS-HFS within the experimental accuracy ±50 V. Figure 9(b) shows 2D potential distribution with the minimal value of potential at the plasma axis. Equipotential lines are consistent with vacuum magnetic flux surfaces.

Figure 10 shows that, similar to the ECRH plasmas, RMS distributions are not fully symmetric. The asymmetry is much less pronounced respect to ECRH, it is maximal near $\rho = 0.2$–0.3, the asymmetry factor is about 1.1 for plasma density, for potential it is almost negligible.

Figure 11 shows radial distribution of the plasma density and potential RMS evolution with density in the scenario with NBI heating started with low-density ECRH. We see that the RMS of core broadband turbulence in higher density NBI plasma (blue and black curves) is reduced by a factor of two in the region ρ < 0.4–0.5, where the density profile is flat, compared to the lower density ECRH plasmas (red curves). At the same time, for the outer region of the density gradient, ρ > 0.5, the broadband density turbulence is higher in NBI phase. This increase is asymmetric: it is stronger in the LFS, up to 1.7–1.8, in contrast to the HFS, where it is below 1.4. Radial distribution of the RMS in the NBI phase depends on the plasma density. In NBI plasmas with lower densities ($\bar{n}_e = 0.9$–1.1×10^{19} m^{-3}) RMS is slightly asymmetric. Similar to ECRH plasmas, RMS at half-radius is enhanced in the HFS by a factor of 1.5 from the level of 0.7%–1% in the LFS. For higher densities ($\bar{n}_e = 1.2$–1.3×10^{19} m^{-3}), RMS is fully symmetric at the minimal level of 0.7%–1% in the core ρ < 0.4–0.5.

Figure 11(b) shows that the plasma potential oscillations, in general, behave similar to the density ones: the total RMS level decreases up to the factor of 2 in the bulk NBI plasmas (ρ < 0.8) with respect to the ECRH level. The RMS level is as low as 6–8 V in this region, while it steeply increases up to 30 V at the very edge ($\rho = 1$).

3.3. *Alfvén eigenmodes*

The density in NBI sustained plasma gradually grows due to the fuelling. The proposed method of 2D mapping allows one to focus on the radial distribution of AE [27, 28]. For mapping, we select shots with reproducible density time traces within the tolerance of less than 5%. Figure 12(a) shows the power

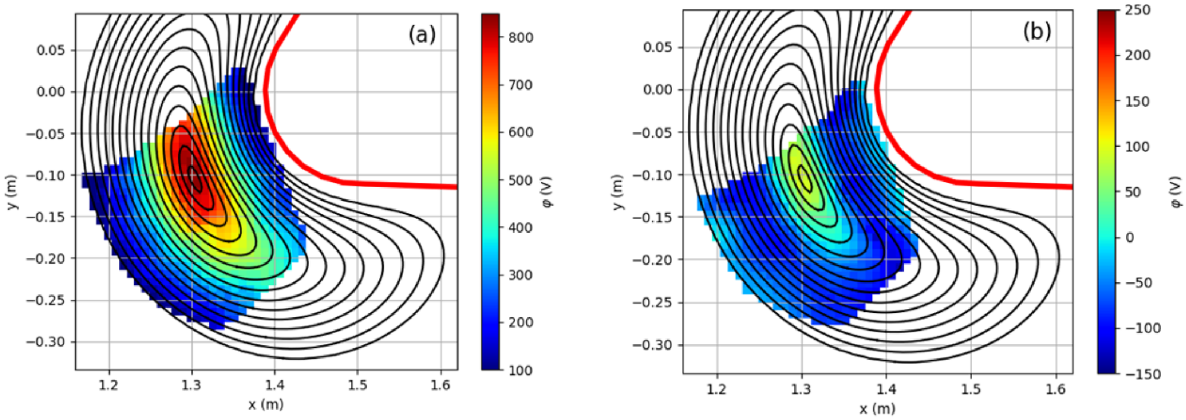

Figure 5. 2D map of mean plasma potential. (a) Stage 1, $P_{\mathrm{EC}} = 470$ kW, $\bar{n}_{\mathrm{e}} = 0.47 \times 10^{19}$ m^{-3}; (b) stage 2, $P_{\mathrm{EC}} = 220$ kW, $\bar{n}_{\mathrm{e}} = 0.78 \times 10^{19}$ m^{-3}. Red curve denotes the chamber wall. Shots ##48 405–48 482.

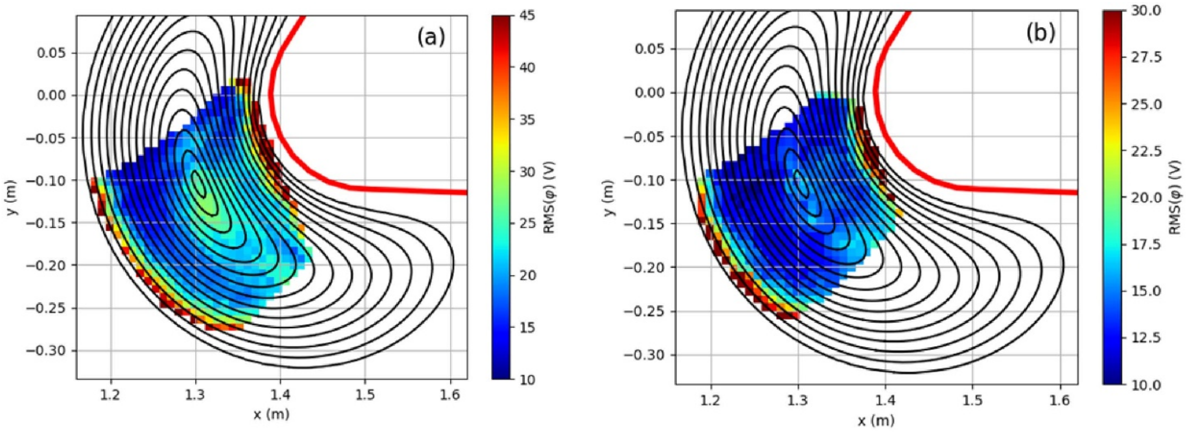

Figure 6. 2D structure of the plasma potential fluctuations. (a) Stage 1, $P_{\mathrm{EC}} = 470$ kW, $\bar{n}_{\mathrm{e}} = 0.47 \times 10^{19}$ m^{-3}; (b) stage 2, $P_{\mathrm{EC}} = 220$ kW, $\bar{n}_{\mathrm{e}} = 0.78 \times 10^{19}$ m^{-3}.

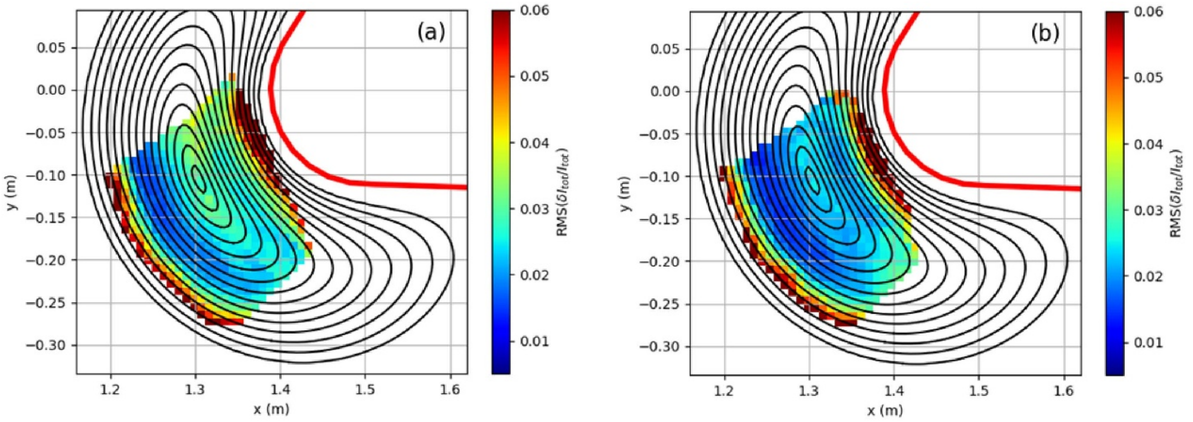

Figure 7. 2D structure of the RMS of density fluctuations. (a) Stage 1, $P_{\mathrm{EC}} = 470$ kW, $\bar{n}_{\mathrm{e}} = 0.47 \times 10^{19}$ m^{-3}; (b) stage 2, $P_{\mathrm{EC}} = 220$ kW, $\bar{n}_{\mathrm{e}} = 0.78 \times 10^{19}$ m^{-3}.

spectrogram of the selected AE on plasma potential, evolving in time according to the plasma density and iota evolution (b), obtained by HIBP in a scanning mode. The mode under study is enclosed by magenta line. Also, figure 12(b) shows the time evolution of the oscillation amplitude, calculated in the marked time-frequency area of AE:

$$A(t) = \sqrt{\frac{2}{f_{\mathrm{Nyq}}} \int_{f_{\min}}^{f_{\max}} S(f,t)\mathrm{d}f},$$

where $S(f,\ t)$ is the Fourier power spectral density, f_{Nyq} is the Nyquist frequency.

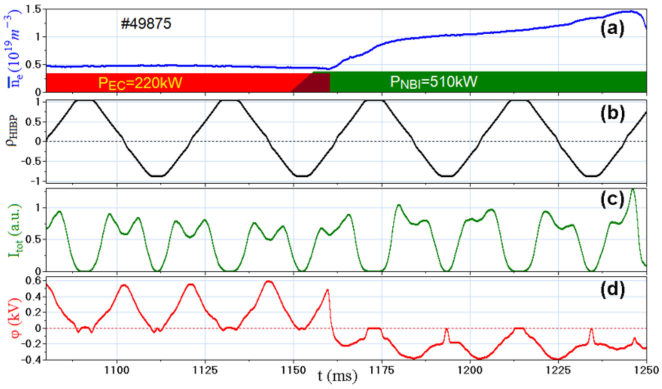

Figure 8. NBI scenario started with ECRH for measurements of 2D maps: (a) line-averaged density; (b) SV position during HIBP scan; (c) secondary HIBP current representing the local density; (d) local plasma potential.

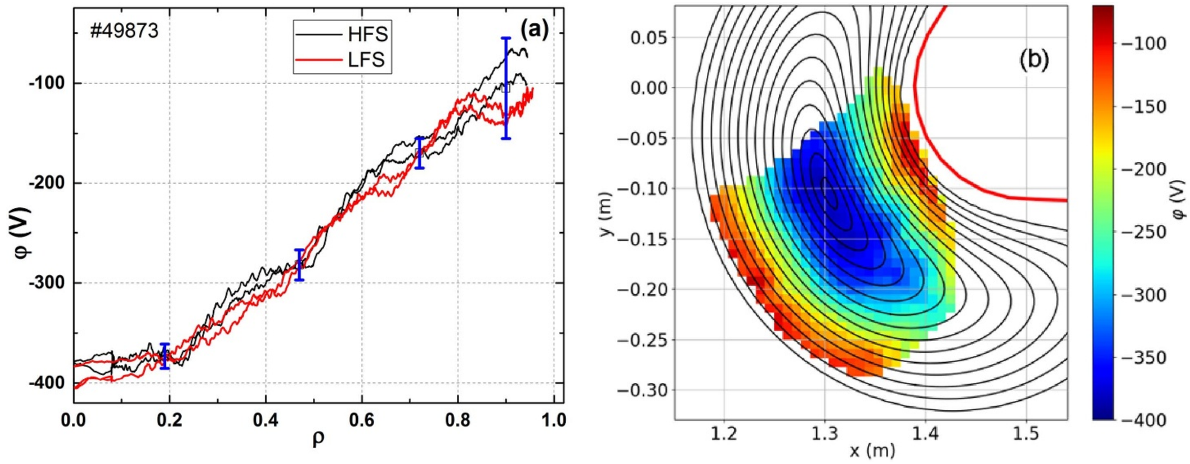

Figure 9. Radial profiles of potential measured along the central detector line $E_b = 132$ keV; blue error bars correspond to RMS (a); and 2D potential contour plot (b) in NBI plasmas: $\bar{n}_e = 0.95–1.2 \times 10^{19}$ m^{-3}.

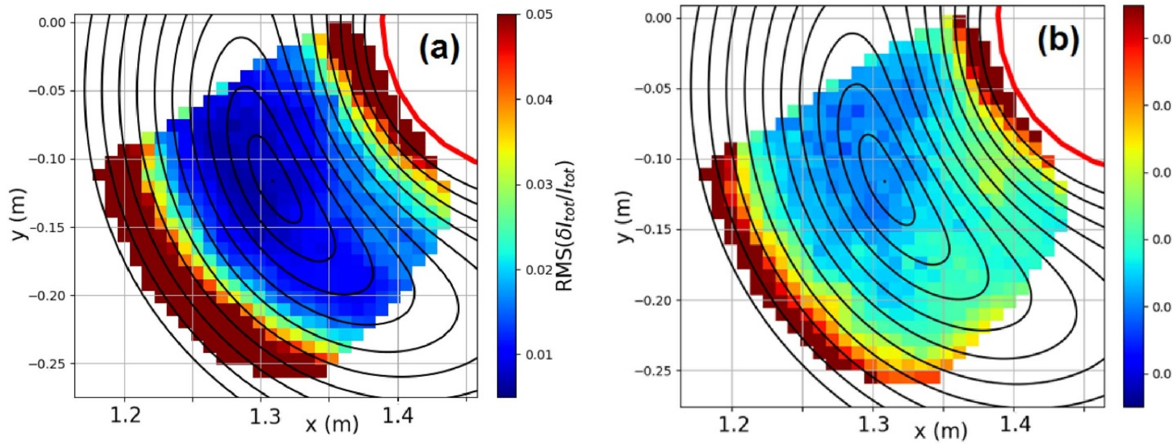

Figure 10. 2D structure of the fluctuations for NBI plasma, $P_{NBI} = 510$ kW, $\bar{n}_e = 0.95–1.2 \times 10^{19}$ m^{-3}; (a) relative density fluctuations; (b) potential fluctuations in kilovolts.

The narrow spikes in this time dependence indicate the time intervals, in which HIBP SV passes the area of AE location. Figure 12(c) shows the power spectral density of potential oscillation in two radial scans, corresponding to AE, and figure 12(d) shows the amplitude and spatial location of the selected mode.

The presented technique of the beam energy variation allows us to reconstruct the spatial distribution of the selected

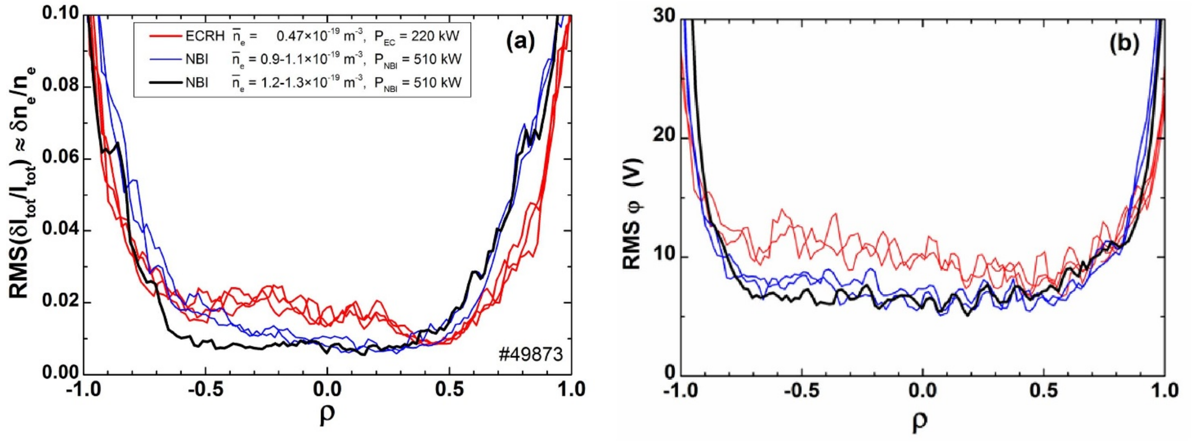

Figure 11. Radial distribution of the RMS of fluctuation ($f < 300$ kHz and poloidal wave vector $k_\omega < 3$ cm^{-1}) for plasma density (a) and potential (b) in ECRH and NBI plasmas.

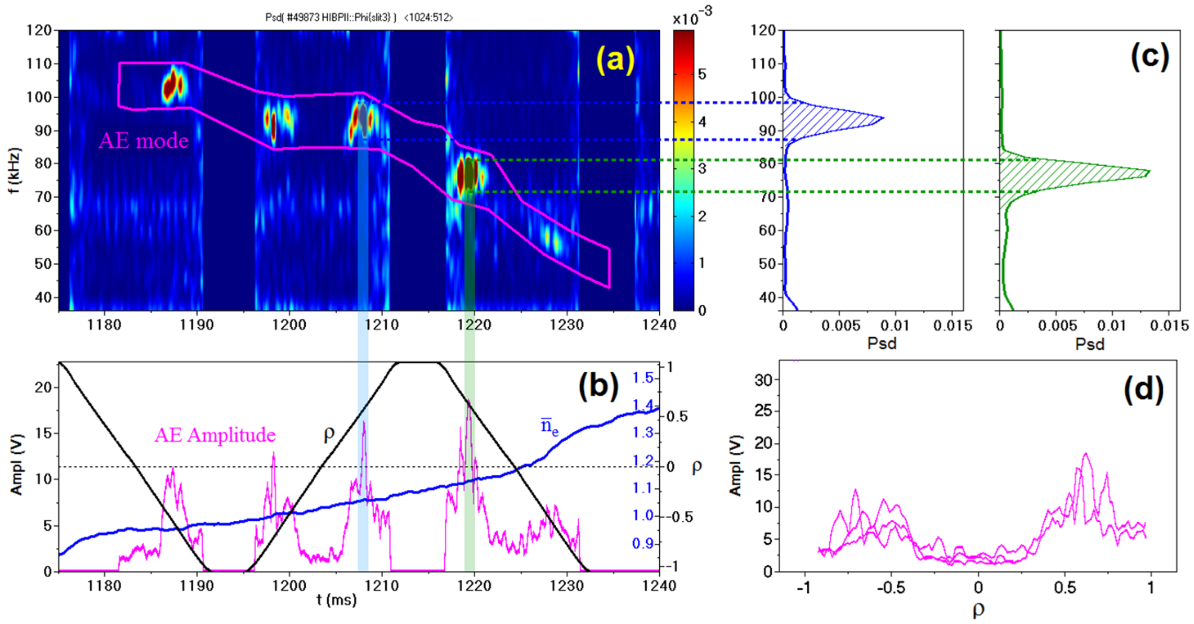

Figure 12. (a) Power spectrogram of potential fluctuations; (b) radial scan of HIBP, ρ, with $E_b = 132$ keV, rising density, $\bar{n}_e$ and calculated amplitude of selected AE; (c) power spectra of selected AE in two time instances, and (d) radial profile of the AE amplitude in several radial scans.

AE mode, as shown in figure 13. We see that the mode amplitude is about 10 V, and it is located at the specific flux surface $\rho = 0.6$ in the plasma vertical cross-section. Note that unless the amplitude of the AE-associated potential perturbation is evolving in time, it has an asymmetric structure, the mode is more pronounced at LFS. Its amplitude is up to 10 V at HFS, while it is up to 17 V in LFS for the mode under discussion.

3.4. Suprathermal electron electrostatic modes

In the very low-density, low-collisionality ECRH plasmas, the electrostatic modes coupled to the suprathermal electrons (ST-modes) may be excited [29]. Figure 14(a) shows the power spectrograms of plasma emission fluctuations measured by the central chord of bolometer in the shot #51 618 with $\bar{n}_e = 0.3$–0.35×10^{19} m^{-3}, $P_{\mathrm{ECRH}} = 540$ kW, $T_e(0) = 1.6$ keV. ST-mode (marked by magenta line) is clearly pronounced as a quasicoherent mode with slightly decreasing frequency around below 75 kHz. Figures 14(b) and (c) show the fluctuating and steady parts of the local density correspondingly, obtained by radial scan of the HIBP secondary beam current. It shows that the ST-mode is localized at the central area, where the hollow density profile has a positive gradient. The technique developed for reconstruction of the AEs spatial distribution was used for the ST-mode. As a result, 2D map of the ST-mode is presented in figure 15. We see that the mode amplitude is above 2.5%, and it is located at the specific flux surface $\rho = 0.25$ in the plasma vertical cross-section. The ST-mode is hardly seen on fluctuations of potential and poloidal magnetic field. Note that in contrast to the AEs, ST-mode has an asymmetry along the vertical direction:

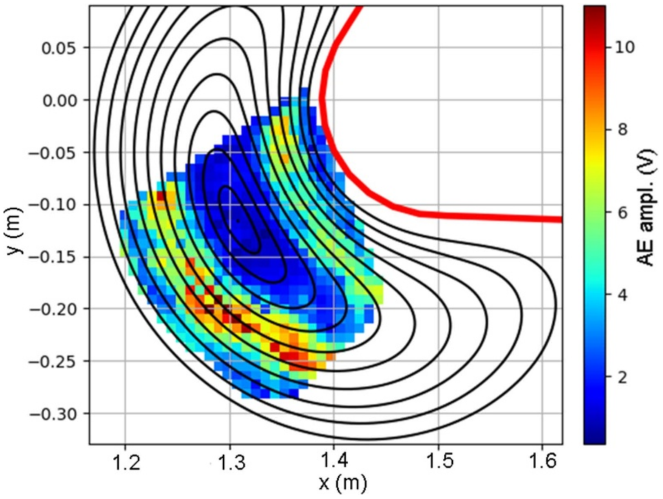

Figure 13. 2D distribution of the AE amplitude in plasma potential measured in shot-by-shot (##49 858–49 880) energy scan, $E_b = 88–150$ keV.

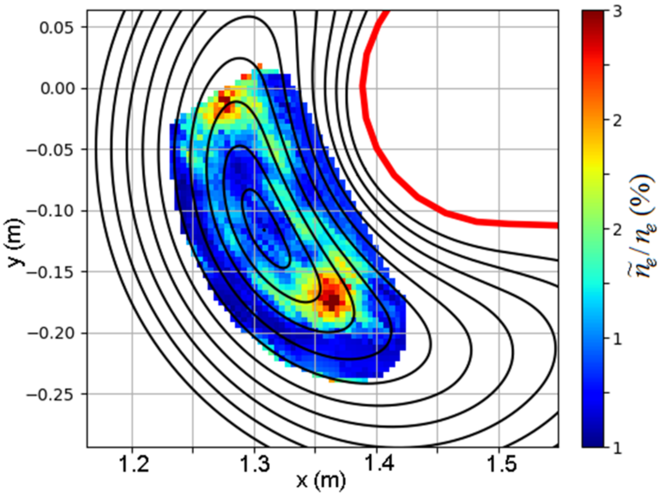

Figure 15. 2D distribution of the ST-mode on the relative density perturbation in percent. Shots ##51 787–51 820.

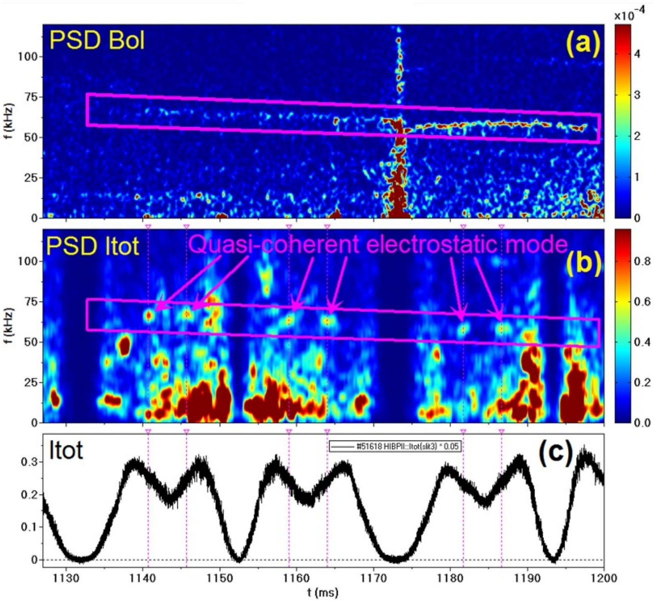

Figure 14. Shot with electrostatic modes driven by the suprathermal electrons. Power spectrograms of (a) plasma emission fluctuations measured by bolometer (AXUV-detector); (b) plasma density fluctuations, represented by HIBP secondary current during the radial scan with $E_b = 132$ keV; (c) the corresponding radial distribution of density (beam current).

the maxima at the top and bottom, and the minima around the equatorial plane.

4. Discussion

Presented paper shows the progress in the knowledge of the physics based on the recent advances in HIBP diagnostics respect to the previous stage [5].

The developed technique appears to be productive for analysis of the mean values and fluctuations. For the series of 15–40 reproducible discharges, it is capable to produce 2D distribution of the plasma potential, and fluctuations of density and potential, so make the imaging of the static structures with lifetime larger than HIBP scanning time (5–10 ms). Technical improvements expand the observable spatial area to about 2/3 of the plasma vertical cross-section from the edge to the centre. HIBP plasma potential profiles become more centred with vacuum magnetic axis, compared to initial data [5], and coincide with the edge potential profile measured by the LP. The potential contour plots show a coincidence with vacuum magnetic flux surfaces over the whole observed area.

The experience of the plasma imaging in TJ-II shows that various structures took place in different plasma regimes. There is really poloidally symmetric distribution for plasma potential. Antiballooning structure is observed for the broadband potential and density oscillations with maximum asymmetry in low-density ECRH plasma. Ballooning structure is a feature of the plasma potential perturbation caused by AE, while $m = 2$-like structure is observed for the density perturbations associated with suprathermal electron mode. Observed antiballooning structure for the potential and density broadband oscillations decreases with density ramp-up in both ECRH and NBI scenarios up to total vanishing in the latter case.

These observations present an important experimental data for the validation of the MHD [30] and GK [31] codes for toroidal plasma devices, which is necessary to improve the reliability of the predictions for operating and future devices.

5. Summary

2D plasma potential distribution was measured in TJ-II for the first time in toroidal fusion devices in a wide area of vertical cross-section in ECRH and NBI plasmas.

In both ECRH and NBI plasmas, equipotential lines are consistent with vacuum magnetic flux surfaces, 2D potential distribution is symmetric (LFS-HFS and up-down) with local extrema at the plasma centre (maximum up to +900 V for

ECRH low-density plasma, minimum up to −300 V for NBI higher density plasma).

In low-density ($\bar{n}_e = 0.5–0.8 \times 10^{19}$ m^{-3}) ECRH plasmas, the potential and density RMS are not fully symmetric, the asymmetry is stronger for lower-density case: at the mid radius (area of the maximum density), the broadband turbulence RMS $\varphi \sim 15$ V at LFS vs ∼20 V at HFS; RMS $n_e \sim 2\%$ at LFS vs ∼3% at HFS. In the NBI plasmas with the density ramp-up, the asymmetry is decreasing and finally vanishing at $\bar{n}_e = 1.2–1.3 \times 10^{19}$ m^{-3}.

2D distribution of the NBI-induced AEs was measured. AEs show asymmetric structures: contrary to the broadband turbulence mode-associated potential perturbations, they dominate in the LFS with a factor up to 1.7 with respect to the HFS.

The electrostatic mode, excited in ECRH plasmas by suprathermal electrons, also shows asymmetric structures: density perturbation dominates in the top-bottom direction compared to LFS-HFS direction.

Data availability statement

All data that support the findings of this study are included within the article (and any supplementary files).

Acknowledgments

This work has been carried out within the framework of the EUROfusion Grant Agreement No. 633053. Kurchatov team was supported by Russian Science Foundation, Project 19-12-00312. A V M was partly supported by Competitiveness program of NRNU MEPhI.

ORCID iDs

A V Melnikov https://orcid.org/0000-0001-6878-7493
J M Barcala https://orcid.org/0000-0002-1092-7091
A Cappa https://orcid.org/0000-0002-2250-9209
C Hidalgo https://orcid.org/0000-0002-0736-7855
P O Khabanov https://orcid.org/0000-0002-6004-2005
D López-Bruna https://orcid.org/0000-0002-7638-8772
U Losada https://orcid.org/0000-0003-1161-8976
S E Lysenko https://orcid.org/0000-0003-1529-2088
A Molinero https://orcid.org/0000-0003-3848-2626
M Ochando https://orcid.org/0000-0001-7521-4503
J L De Pablos https://orcid.org/0000-0002-3850-0196
I Pastor https://orcid.org/0000-0003-0891-0941

References

[1] Hidalgo C 1995 Edge turbulence and anomalous transport in fusion plasmas *Plasma Phys. Control. Fusion* **37** A53
[2] Xanthopoulos P *et al* 2016 Intrinsic turbulence stabilization in a stellarator *Phys. Rev.* X **6** 021033
[3] García-Regaña J M *et al* 2018 On-surface potential and radial electric field variations in electron root stellarator plasmas *Plasma Phys. Control. Fusion* **60** 104002
[4] Angioni C, Lang P T and Manas P 2017 Density gradient driven microinstabilities and turbulence in ASDEX Upgrade pellet fuelled plasmas *Nucl. Fusion* **57** 116053
[5] Sharma R *et al* 2020 Measurements of 2D poloidal plasma profiles and fluctuations in ECRH plasmas using the heavy ion beam probe system in the TJ-II stellarator *Phys. Plasmas* **27** 062502
[6] Estrada T *et al* 2019 Turbulence and perpendicular plasma flow asymmetries measured at TJ-II plasmas *Nucl. Fusion* **59** 076021
[7] Eliseev L G *et al* 2021 2D distributions of potential and density mean-values and oscillations in the ECRH and NBI plasmas at the TJ-II stellarator *28th IAEA Fusion Energy Conf. (FEC 2020)* (*10–15 May 2021*) pp EX/P6–17 (available at: https://nucleus.iaea.org/sites/fusionportal/Shared%20Documents/FEC%202020/fec2020-preprints/preprint0680.pdf)
[8] Sánchez E, Estrada T, Velasco J L, Calvo I, Cappa A, Alonso A, García-Regaña J M, Kleiber R and Riemann J 2019 Validation of global gyrokinetic simulations in stellarator configurations *Nucl. Fusion* **59** 076029
[9] Fujisawa A 2003 Experimental studies of structural bifurcation in stellarator plasmas *Plasma Phys. Control. Fusion* **45** R1–R88
[10] Fujisawa A, Ouroua A, Heard J W, Crowley T P, Schoch P M, Connor K A, Hickok R L and Wootton A J 1996 Ballooning characteristics in density fluctuations observed with the 2 MeV heavy ion beam probe on the TEXT-U tokamak *Nucl. Fusion* **36** 375
[11] Watts C *et al* 1996 Poloidal asymmetry and gradient drive in core electron density and temperature fluctuations on the Texas experimental tokamak-upgrade *Phys. Plasmas* **3** 2013
[12] Shimizu A, Ido T, Nishiura M, Kato S, Ogawa K, Takahashi H, Igami H, Yoshimura Y, Kubo S and Shimozuma T 2016 2D spatial profile measurements of potential fluctuation with heavy ion beam probe on the large helical device *Rev. Sci. Instrum.* **87** 11E731
[13] Hidalgo C *et al* 2005 Overview of TJ-II experiments *Nucl. Fusion* **45** S266
[14] Melnikov A V 2019 *Electric Potential in Toroidal Plasmas* (*Springer Series in Plasma Science and Technology*) ed S E Lysenko (Cham: Springer) pp 1–240
[15] Melnikov A V *et al* 2018 ECRH effect on the electric potential and turbulence in the TJ-II stellarator and T-10 tokamak plasmas *Plasma Phys. Control. Fusion* **60** 084008
[16] Melnikov A V *et al* 2010 Study of Alfvén eigenmodes in the TJ-II stellarator *Plasma Fusion Res.* **5** S2019
[17] Van Milligen B P, Estrada T, Jiménez-Gómez R, Melnikov A, Hidalgo C, Fontdecaba J M, Krupnik L, Eliseev L G and Perfilov S V 2011 A global resonance phenomenon at TJ-II stellarator *Nucl. Fusion* **51** 013005
[18] Melnikov A V *et al* 2015 Control and data acquisition for dual HIBP diagnostics in the TJ-II stellarator *Fusion Eng. Des.* **96–97** 724
[19] Alonso J A *et al* 2017 Observation of oscillatory radial electric field relaxation in a helical plasma *Phys. Rev. Lett.* **118** 185002
[20] Krupnik L I *et al* 2020 High-intensity cesium ion beams for HIBP diagnostics *Probl. At. Sci. Technol.: Ser. Plasma Phys.* **26** 190
[21] Melnikov A V *et al* 2017 Heavy ion beam probing—diagnostics to study potential and turbulence in toroidal plasmas *Nucl. Fusion* **57** 072004
[22] Ross D W, Sloan M L, Wootton A J, Schoch P M, Heard J W, Crowley T P, Hickok R L and Simcic V 1992 Effect of beam-attenuation modulation on fluctuation measurements by heavy-ion beam probe *Rev. Sci. Instrum.* **63** 2232

[23] Melnikov A V *et al* 2016 Study of NBI-driven chirping mode properties and radial location by the heavy ion beam probe in the TJ-II stellarator *Nucl. Fusion* **56** 112019

[24] Melnikov A V *et al* 2007 Plasma potential evolution study by HIBP diagnostic during NBI experiments in the TJ-II stellarator *Fusion Sci. Technol.* **51** 31

[25] García L, Ochando M A, Carreras B A, Carralero D, Hidalgo C and van Milligen B P 2016 Effect of fast electrons on the stability of resistive interchange modes in the TJ-II stellarator *Phys. Plasmas* **23** 062319

[26] Khabanov P O *et al* 2019 Density profile reconstruction using HIBP in ECRH plasmas in the TJ-II stellarator *J. Instrum.* **14** C09033

[27] Melnikov A V *et al* 2010 Internal measurements of Alfvén eigenmodes with heavy ion beam probing in toroidal plasmas *Nucl. Fusion* **50** 084023

[28] Jiménez-Gómez R *et al* 2011 Alfvén eigenmodes measured in the TJ-II stellarator *Nucl. Fusion* **51** 033001

[29] Melnikov A V *et al* 2011 A quasi-coherent electrostatic mode in ECRH plasmas on TJ-II *Plasma Fusion Res.* **6** 2402030

[30] Milligen B P *et al* 2021 Topology of 2D turbulent structures based on intermittence in the TJ-II stellarator *Nucl. Fusion* **61** 116063

[31] Hidalgo C *et al* 2022 Overview of the TJ-II stellarator research programme towards model validation in fusion plasmas *Nucl. Fusion* **62** accepted